Karakoc, Alp; Sjölund, Johanna; Reza, Mehedi; Freund, Jouni; Hernandez-Estrada, Albert; Paltakari, Jouni

Modeling of wood-like cellular materials with a geometrical data extraction algorithm

Published in:
Mechanics of Materials

DOI:
10.1016/j.mechmat.2015.10.019

Published: 01/02/2016

Document Version
Peer-reviewed accepted author manuscript, also known as Final accepted manuscript or Post-print

MODELLING OF WOOD-LIKE CELLULAR MATERIALS WITH A GEOMETRICAL DATA EXTRACTION ALGORITHM

Alp Karakoç*[,1], Johanna Sjölund[2], Mehedi Reza[3], Jouni Freund[2], Albert Hernandez Estrada[1], Jouni Paltakari[1]

[1] Aalto University, School of Chemical Technology, Department of Forest Products Technology, P.O.BOX 16300, FI-00076 AALTO, FINLAND

[2] Aalto University, School of Engineering, Department of Applied Mechanics, P.O.BOX 14300, FI-00076 AALTO, FINLAND

[3] Aalto University, School of Science, Department of Applied Physics, P.O.BOX 11100, FI-00076 AALTO, FINLAND

ABSTRACT

An algorithm on geometrical data extraction, material reconstruction and numerical analysis is presented in order to reconstruct the actual wood-like cellular materials and investigate their linear elastic material behaviour in the transverse plane under different loading conditions. The algorithm implemented by Mathematica technical computing software is used to read the pixel data of cellular material images with a wide range of material scales, e.g. from micro- to millimeter scale. As a result of this process, geometrical properties including cell wall thicknesses, cell connectivities, vertex and center coordinates are determined. Identified geometrical properties are transferred to Abaqus/CAE computer aided engineering software by using a Python script and also

converted into stereolithography STL model format enabling prototype generation and visualization. As an application example, the reconstructed model by means of the algorithm was used to investigate the in-plane effective stiffness properties of Norway spruce earlywood specimens in the frameworks of homogenization and finite element analysis.

Keywords: *material reconstruction*, *cellular material*, *stereolithography STL*, *in-plane effective stiffness*, *Norway spruce, finite element analysis*.

* Corresponding author. Tel: +358 50 344 2937.
Email address: alp.karakoc@alumni.aalto.fi (Alp Karakoç).

1. INTRODUCTION

The increasing computation power, and emerging image processing and reconstruction technologies have given rise to the investigation and visualization of the geometrical and mechanical properties of materials. Especially in the field of cellular material science, these technologies can provide accurate geometrical data for mechanical analysis and insight into modeling and design procedures [Farrugia and Perre, 2000; Magne, 2007]. As a result, modeling errors due to geometrical input can be reduced and accuracy of the simulation experiments can be enhanced.

Yet studies on cellular materials do not widely use the image processing technologies to

determine the material geometry and use it as an input for simulation experiments. The conventional approach follows the representation of the whole material with regular repetitive unit elements, i.e. hexagonal, rectangular, etc., and investigations into the mechanical behaviour of these elements [Gibson and Ashby, 1997; Qing and Mishnaevsky, 2011; Freund et al., 2014]. Although results out of this approach can be regarded satisfactory, modeling errors due to fictitious geometrical input are inevitable. In the literature, there are successfully conducted studies that use the data extraction and image reconstruction algorithms to determine geometrical input for the material models and simulations. Such studies benefit the accuracy of electron and transmission electron microscopy, nuclear magnetic resonance NMR imaging, X-ray projection, synchrotron radiation X-ray tomography and micro computed tomography, especially in aerospace, biological, agricultural, medical and dental applications [Kahle and Woodhouse, 1994; Cattaneo et al., 2001; Verdonschot et al., 2001; Badel and Perre, 2003; Zdunek et al., 2004; Nguyen et al., 2012; Karakoç and Freund, 2013; Rafsanjani et al., 2012]. Despite the high accuracy of these techniques, expensive equipment and maintenance, sophisticated algorithms and lack of qualified labour obstruct their extensive usage in many engineering applications.

As its novelty, the present algorithm provides a low equipment and labour cost solution to visualize and investigate the geometrical and mechanical characteristics of cellular media. The algorithm is capable of extracting geometrical data and reconstructing cellular materials within a wide range of material scales, e.g. micro- to millimeter scales. In addition, the algorithm also brings appropriate geometrical input parameters for

multiscale characterization of arbitrary cell collections in two dimensional space. Hence, it is possible to estimate the in-plane effective mechanical properties of cellular materials through the material description at the cell scale in the frameworks of homogenization and finite element analysis.

In the present study, first, the sequence of the algorithm is introduced and the principles are explained. Thereafter, an application example is provided, for which two-dimensional micrographs of Norway spruce specimens were captured with optical microscopy as depicted in Fig. 1. In this example, earlywood cross-sections of Norway spruce specimens in the transverse plane was investigated, for which image processing, stereolithographic STL modeling and finite element analysis were used. The accuracy of the proposed algorithm was tested in terms of the empirical and computed effective stiffnesses for Norway spruce earlywood available in the literature.

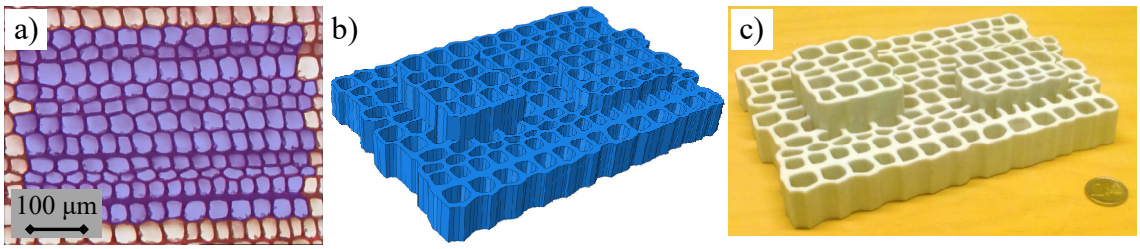

Figure 1: a) Norway spruce earlywood cross-section and region of interest with transparent coloring, b) extruded near-exact model of the region in STL format, c) corresponding three dimensional print.

2. MATERIALS AND METHODS

2.1. Algorithm sequence

The introduced algorithm follows the sequence described in Fig. 2. The starting point is to scan the cellular material layer in the plane of interest and to binarize the image. The binarization data is then used to extract the geometrical information of the cellular structure. The geometrical information is used to form so called near-exact STL models in the present study, which are then used to generate mesh for finite element analysis and prototypes for additive manufacturing. These prototypes are helpful to visualize and understand the geometrical models and details.

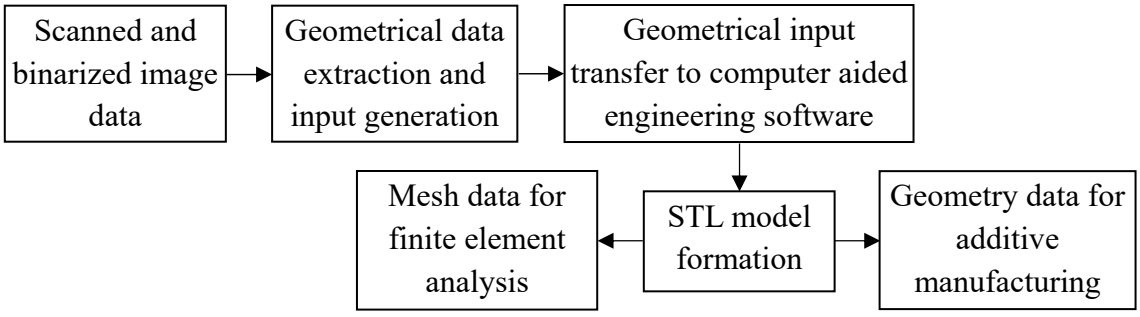

Figure 2: Algorithm sequence.

2.2. Geometrical data extraction algorithm

The proposed geometrical data extraction and input generation algorithm is an automated set operation coded in Mathematica technical computing software. The algorithm extracts

the near-exact features of the cellular material including the cell centroids and vertices, cell wall heights h and thicknesses t as illustrated in Fig. 3. Once these geometrical features are known, it is possible to reconstruct models from image to insight for visual inspections, material prototyping and numerical analyses.

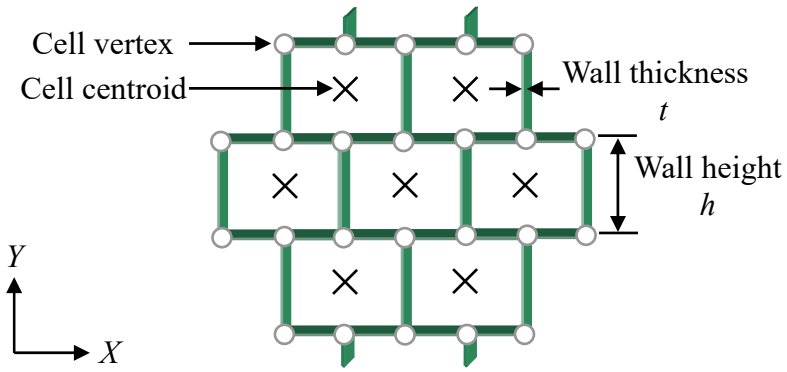

Figure 3: Schematic representation of geometrical features for a cellular material in the transverse plane.

As the initial step, image of the actual undeformed cellular material is captured and binarized in order to obtain foreground and background pixel data. For binarization threshold, Otsu method is used, which minimizes the combined spread of foreground and background pixels. As seen in Fig. 4, foreground pixel data represented with the white color describe the regions inside the cells and background pixel data represented with black color describe the cell walls. After binarization, morphological analysis is performed to define each cell region and coordinates of cell centroids for the i^{th} cell are computed as

$$(X_i, Y_i) = \frac{1}{n}\left(\sum_{j=1}^{n} x_j, \sum_{j=1}^{n} y_j\right), \quad (1)$$

in which (x_j, y_j) are the coordinates of j^{th} foreground pixel and n is the total number of foreground pixels in the i^{th} cell as shown in Fig. 4.

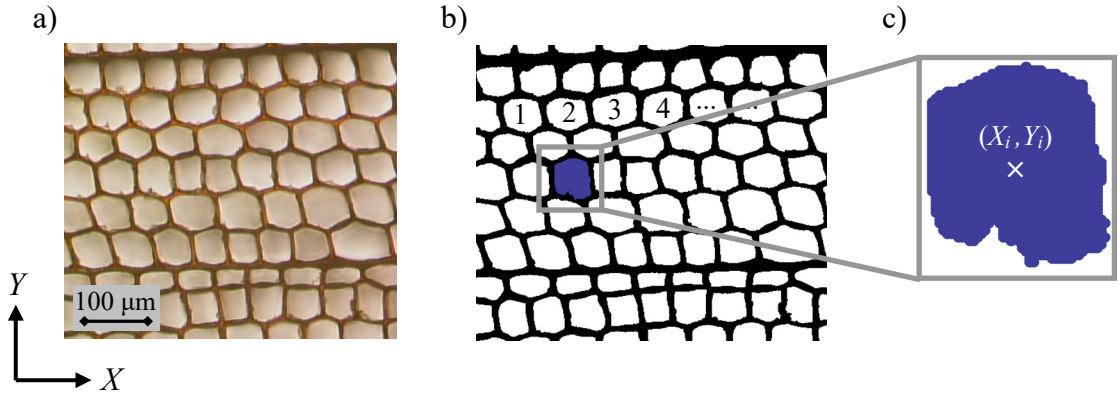

Figure 4: Image processing: a) original image, b) binary image with selected foreground pixels in the cell form, c) cell centroid.

This step is followed by determination of the cell vertices. For this purpose, the centroids in Eq. (1) are sorted based on the minimum Euclidean distance criterion within the framework of k^{th}-nearest neighbor method. The k value highly depends on the cell topology z referring to the connectivity of adjacent cells as shown in Fig. 5 [Silva and Gibson, 1997].

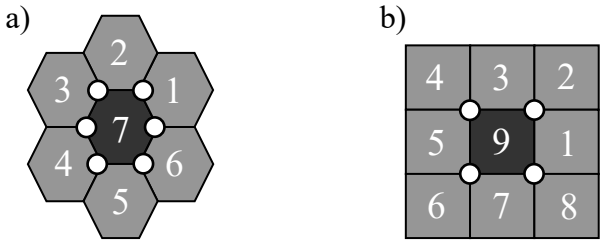

Figure 5: Nearest neighbors and cell topologies used in the present geometric input generation: a) hexagons with k=7 and z=3, b) rectangles with k=9 and z=4.

For instance, for the cross-section shown in Fig. 6, k=9 and z=3, which makes it possible to find all neighboring cells and vertices. The possible cell combination for i^{th} cell is hence given as

$$C_i(k,z) = \frac{k!}{z!(k-z)!} \tag{2}$$

Cell vertex coordinates are detected by using the intersection operations among the neighboring cell combinations of Eq. (2), which is also depicted in Fig. 6. In this setup, it is possible that one can end up with two close points representing the same vertex. Here, close points mean two points, Euclidean distance of which are smaller than the predefined threshold value δ. In this case, these two close points are simply combined by averaging their coordinate data.

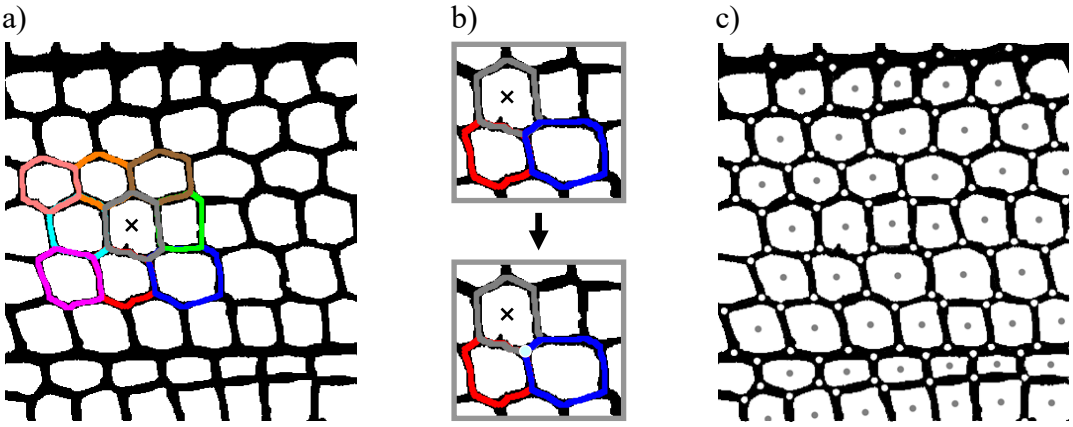

Figure 6: Cell vertex formation through intersection operation: a) k=9 nearest neighbor of a cell depicted with ×, b) intersection of z=3 neighboring cells forming the cell vertex, c) representation of cell vertices with white dots and centroids with gray dots.

After computing the vertex coordinate data, height of each cell wall, h, is determined as the Euclidean distance between two consecutive vertices that belong to the same cell. The cell wall thickness, t, is obtained in such a way that the Euclidean distances between one cell vertex and its nearest foreground pixels of the neighboring cells are computed, which culminates in a circle of radius r around this particular vertex. Once the same procedure is performed for the consecutive vertex, t of the edge formed by these two consecutive vertices is calculated by averaging the computed radii as shown in Fig. 7. The coordinate and dimension data for each cell are then listed for material reconstruction and numerical analysis.

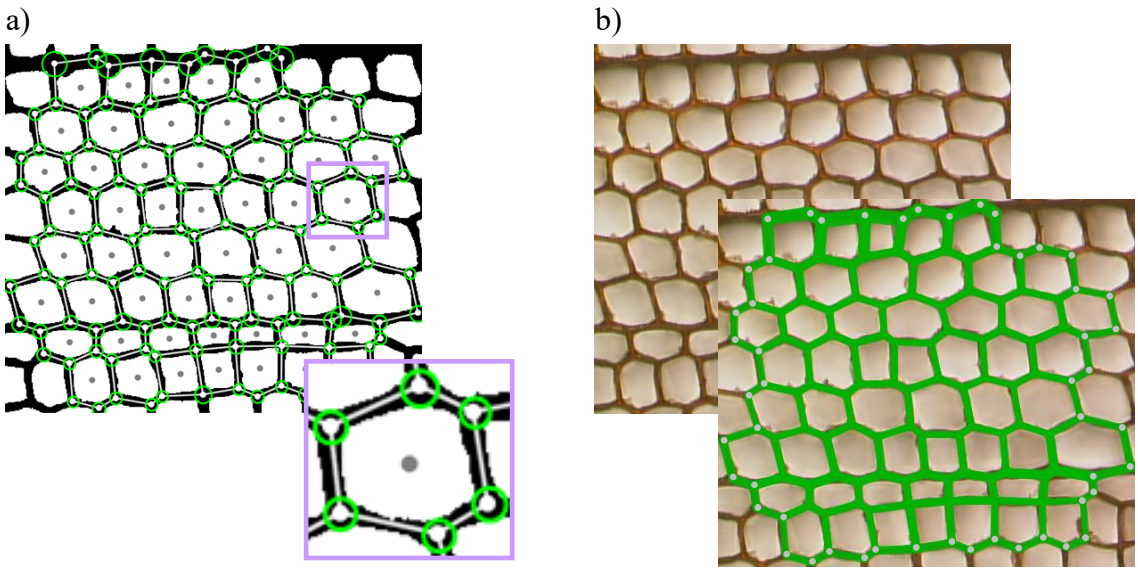

Figure 7: Geometric input: a) representation of the cell bounds with white lines and the cell wall thicknesses by averaging the radii of the circles with centers located at the cell vertices, b) actual and mimicked cellular structure.

2.3. Geometrical data transfer through STL models

2.3.1. STL models in a nutshell

Stereolithographic STL models have been used as a standard geometrical model for surface representation in solid modeling and additive manufacturing. It was first introduced by 3D Systems in 1989 and has been widely used in computer aided drawing and manufacturing [Tian, 2013]. STL models represent the solid surface with triangular elements and the model files are usually in binary or ASCII formats, the difference between which is just based on the data expression method [Iványi, 2012].

2.3.2. Near-exact STL models

The extracted geometrical data, as explained above, are transferred to Abaqus/CAE computer aided engineering software so as to use its STL model generation toolbox and numerical analysis features. The data are transferred with a Python script given in Appendix A, which includes the sketch size information, coordinate data of the exterior and interior nodes for the cells and extrusion information. Sequence of the process is depicted in Fig. 8.

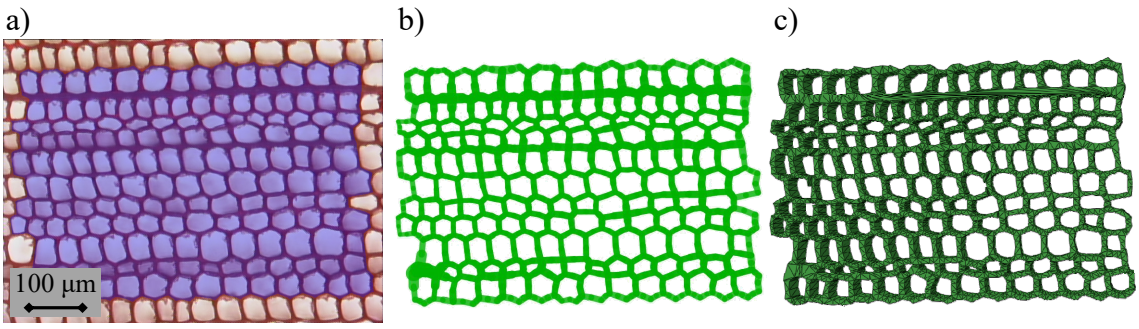

Figure 8: a) Region of interest represented with transparent coloring in a wood-like cellular material, b) extracted geometry in the transverse plane by Mathematica technical computing software and c) near-exact STL model generated in Abaqus/CAE computer aided engineering software.

2.4. Homogenization framework

2.4.1. Strain driven computational homogenization

Strain driven computational homogenization is a numerical multiscale method, which has been widely used to estimate the effective stiffness properties [Sjölund et al., 2015]. In this method, macroscopic strain e_{ij}^{M} for $i, j \in \{X, Y, Z\}$ is assumed to be uniform over the material and imposed at a representative volume element RVE boundary $\partial\omega$ containing enough information to describe material behavior as illustrated in Fig. 9. Therefore, microscopic displacement field decomposition for RVE can be given as

$$\vec{u}^{\,\mathrm{m}} = \vec{r} \cdot \mathbf{e}^{\mathrm{M}} + \underline{\vec{u}}, \tag{3}$$

for which superscripts m and M stand for microscopic and macroscopic scales, and the first addend on the right hand side represents the macroscopic displacement contribution and second addend represents the displacement fluctuation field $\underline{\vec{u}}$ due to heterogeneities within the RVE. Here, $\vec{r}$ represents the position vector with respect to any described origin.

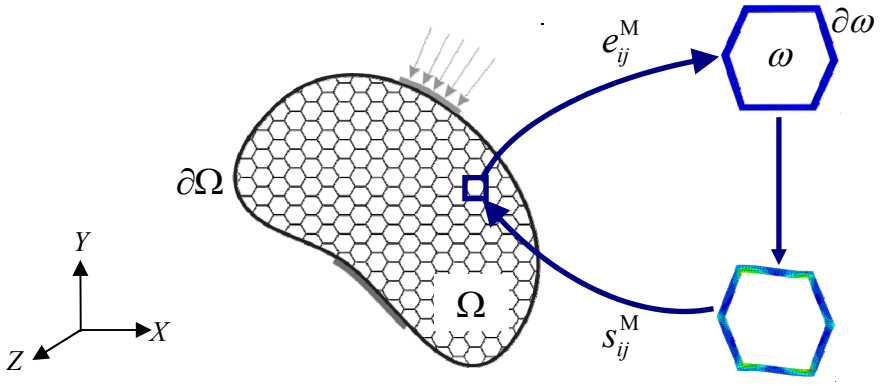

Figure 9: A strain driven homogenization scheme with imposed macroscopic strain e_{ij}^{M} and computed stress s_{ij}^{M} for $i, j \in \{X, Y, Z\}$. Here, Ω and $\partial\Omega$ represents the volume and boundary of aggregate, and ω *and* $\partial\omega$ represents the volume and boundary of RVE.

Here, continuity conditions of the displacements and tractions must be satisfied at the RVE boundaries. The first condition can be satisfied by taking the relative positions of the node sets, e.g. node 1 and node 2 at the boundaries, i.e. surfaces, edges, corners. Hence, Eq. (3) can be expanded as

$$\vec{u}_1^{\mathrm{m}} - \vec{u}_2^{\mathrm{m}} = \left(\vec{r}_1 - \vec{r}_2\right) \cdot \mathbf{e}^{\mathrm{M}}, \tag{4}$$

where the displacement fluctuation field $\vec{u}$ of Eq. (3) vanishes under the periodicity condition. The traction boundary condition is satisfied with anti-periodicity of traction field in case of existence of traction on the boundaries [Nguyen et al., 2012]. However, the current study focuses on the displacement boundary conditions; therefore, only Eq. (4) is studied.

2.4.2. Hill-Mandel principle and stress averaging

Hill-Mandel principle establishes and guarantees the energy consistency between the micro- and macroscopic material scales such that [Sjölund et al., 2015]

$$\mathbf{s}^{\mathrm{M}} : \mathbf{e}^{\mathrm{M}} = \frac{1}{\omega}\int_{\omega} \mathbf{s}^{\mathrm{m}} : \mathbf{e}^{\mathrm{m}}\, \mathrm{d}\omega, \tag{5}$$

for which ω *and* $\partial\omega$ represents the volume and boundary of RVE as also depicted in Fig. 9. The symbol (:) denotes the double dot operator and for second order tensors it is defined as

$$\mathbf{a} : \mathbf{b} = a_{ij} b_{ij}. \tag{6}$$

By using the Gauss theorem, Eq. (5) can be rewritten at the RVE boundary $\partial\omega$ as

$$\mathbf{s}^{\mathrm{M}} : \mathbf{e}^{\mathrm{M}} = \frac{1}{\omega}\int_{\partial\omega} \vec{t}^{\,\mathrm{m}} \cdot \vec{u}^{\,\mathrm{m}}\, \mathrm{d}\partial\omega, \tag{7}$$

where $\vec{t}^{\,\mathrm{m}}$ is the microscopic traction vector at $\partial\omega$. By plugging Eq. (3) into Eq. (7),

$$\mathbf{s}^{\mathrm{M}} : \mathbf{e}^{\mathrm{M}} = \frac{1}{\omega}\int_{\partial\omega} \left(\vec{t}^{\,\mathrm{m}} \otimes \vec{r}\right) \mathrm{d}\partial\omega : \mathbf{e}^{\mathrm{M}} + \frac{1}{\omega}\int_{\partial\omega} \vec{t}^{\,\mathrm{m}} \cdot \underline{\vec{u}}\, \mathrm{d}\partial\omega. \tag{8}$$

Here, the symbol $\otimes$ denotes the dyadic operator. The second integrand at the right hand side vanishes in case of periodic boundary conditions as elaborated in Eq. (4). Hence, macroscopic stress $\mathbf{s}^{\mathrm{M}}$ can be expressed as the volume average of the microscopic stress $\mathbf{s}^{\mathrm{m}}$ such that

$$\mathbf{s}^{\mathrm{M}} = \frac{1}{\omega}\int_{\partial\omega} \left(\vec{t}^{\,\mathrm{m}} \otimes \vec{r}\right) \mathrm{d}\partial\omega = \frac{1}{\omega}\int_{\omega} \mathbf{s}^{\mathrm{m}}\, \mathrm{d}\omega, \tag{9}$$

in which ω is the total volume of the RVE.

2.4.3. Numerical implementation of strain driven computational homogenization

Similar to geometrical data transfer and model generation described in Section 2.3.2, the strain driven computational homogenization can be also implemented in Abaqus/CAE. The implementation consists of three sub-operations: pre-processing, processing and post-processing as depicted in Fig. 10. The pre-processing has three major functions: material reconstruction, meshing and boundary condition formation. For meshing, extracted material geometry is first discretized and then finite elements, e.g. 6-noded quadratic triangular elements, are used. The boundary conditions are applied onto the nearest neighboring nodes on the opposing boundaries, which follows Eq. (4) with initially known macroscopic strain $\mathbf{e}^{M}$. During the processing, the problem is solved with the finite element solver of Abaqus/CAE. In postprocessing, microscopic stresses $\mathbf{s}^{m}$ and volumes are calculated at each integration point. In order to numerically compute the integration on the right hand side of Eq. (9), microscopic stresses and volumes of the same integration points are first multiplied and then all the multiplication results are summed up. The summation is then divided by the total volume ω computed through the extracted nodal coordinate data, resulting in the macroscopic stress $\mathbf{s}^{M}$ of Eq. (9).

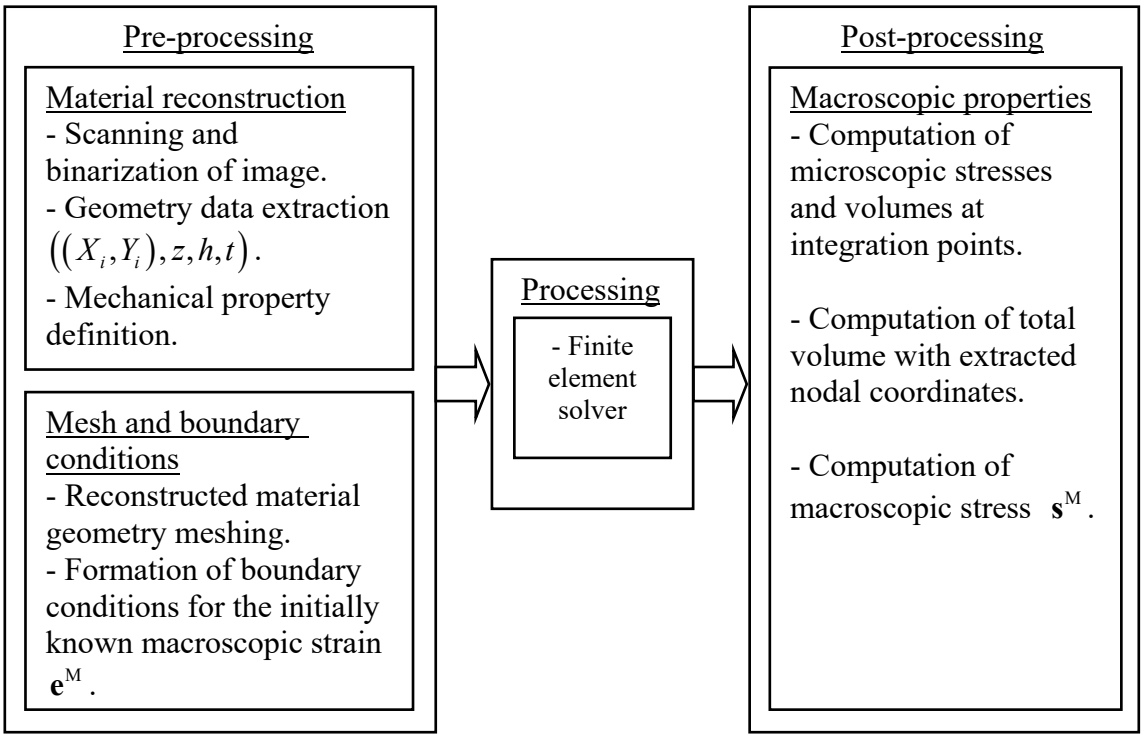

Figure 10: Algorithm sequence for numerical implementation of strain driven computational homogenization.

3. APPLICATION EXAMPLE OF THE ALGORITHM

3.1. Simulation experiments on the stiffness of Norway spruce specimens

In the present study, specimens were taken from the outer stem of mature Norway spruce where the anatomical structure was assumed to be orthotropic. Micrographs were obtained with optical microscope (Nikon Optishot 2, Nikon Europe B.V., Badhoeverdorp, The Netherlands) and maximum resolution of 0.5 μm/pixel. Thereafter, the proposed algorithm was implemented to conduct simulation experiments to understand the material behavior and compute the elastic properties of Norway spruce

earlywood specimens, some of which are shown in Fig. 11. In total, 11 specimens were investigated for defining the elastic property range.

For the simulation experiments, first, STL models were generated by using the micrographs and used as elastic continua in two dimensional space, which were discretized into a set of 6-node quadratic triangular finite elements CPS6 provided in Abaqus/CAE software [ABAQUS, 2004]. Cell walls were taken to be transversely isotropic under the assumption of uniform distribution of cell wall material in the plane of interest. The detailed information of the assumption and supporting empirical data can be found in the literature [Astley et al., 1998]. Hence, mechanical parameters of the cell walls were taken to be E_s=9 GPa and ν_s=0.4 as provided in the previous studies [Kahle and Woodhouse, 1994].

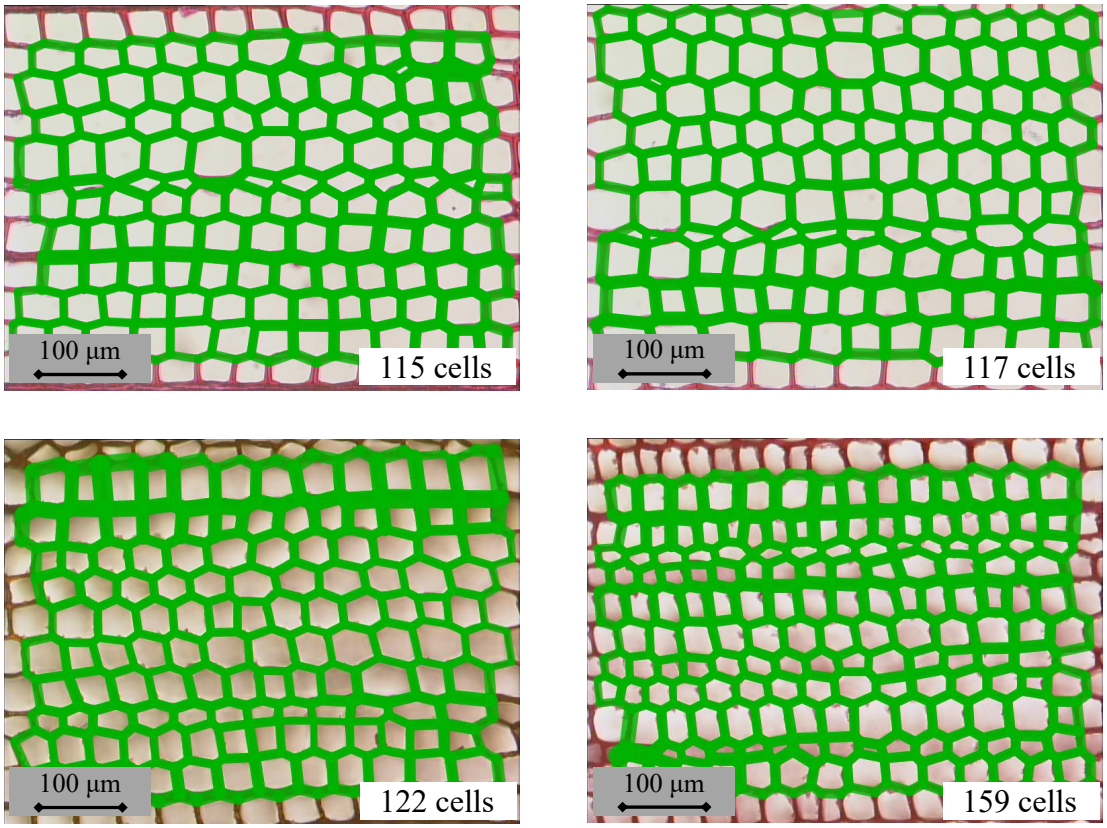

Figure 11: Original images and reconstructed geometries (drawn with green lines) of selected earlywood sections. Number of cells are computed through the extracted geometries representing the simulation solution domain.

Due to limited focal range of the optical microscopy and image acquisition system, it was only possible to investigate small amount of cells in the earlywood. Therefore, boundary constraints were selected to be periodic in the framework of finite element analysis. Hence, the studied elastic continua were assumed to be repeating itself and mimicking an infinite solution domain, for which the idea is based on constraint equations linking the nodal displacements on the opposing edges for planar cases [Kassem and Weichert, 2009]. Inaccuracies are very likely in this type of computation

process due to so called “edge effects” diminishing as the number of cells in earlywood increases [Astley et al., 1998]. For the analyzed specimens, the number of the cells were computed to vary in a range of 114-176. Fig. 12 presents the planar loadings, i.e. tensile loads along *X*- and *Y*-directions and *XY*-shear load, applied on a near-exact model with 159 cells under the given loading and boundary conditions.

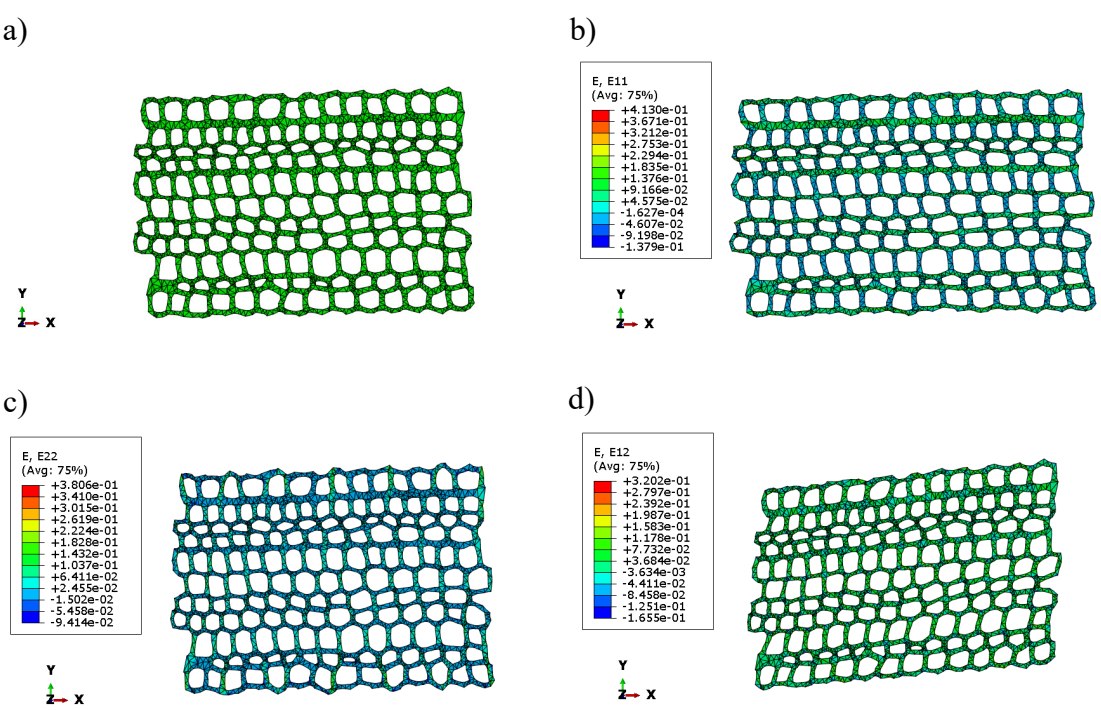

Figure 12: Simulation experiments on near-exact model: a) initial state, b) tensile load along *X*-direction, c) tensile load along *Y*-direction and d) shear load in the *XY*-plane.

Strains $e_{ij}; i,j \in \{X,Y\}$ and stresses $s_{ij}; i,j \in \{X,Y\}$ obtained from the simulations were related under linear elasticity as

$$\mathbf{e} = \mathbf{C} : \mathbf{s}\,, \tag{10}$$

where **C** is the compliance. Despite the compactness of the expression, high-order tensors cause practical difficulties in compliance computations. Thus, for possible numerical computation, Eq. (10) is reconstructed as a matrix operation by using Voigt notation as

$$[\mathbf{C}] = \begin{bmatrix} e^1_{XX} & e^2_{XX} & e^3_{XX} \\ e^1_{YY} & e^2_{YY} & e^3_{YY} \\ 2e^1_{XY} & 2e^2_{XY} & 2e^3_{XY} \end{bmatrix} \begin{bmatrix} s^1_{XX} & s^2_{XX} & s^3_{XX} \\ s^1_{YY} & s^2_{YY} & s^3_{YY} \\ s^1_{XY} & s^2_{XY} & s^3_{XY} \end{bmatrix}^{-1}, \tag{11}$$

for which $[\mathbf{C}]$ is the compliance matrix and superscripts 1, 2 and 3 represents three different loading conditions, i.e. tensile loads along *X*- and *Y*-directions and *XY*-shear load as also depicted in Figure 12. Therefore, it is possible to compute the full compliance matrix including shear modulus. Hence, under the assumption of orthotropic material properties,

$$[\mathbf{C}] = \begin{bmatrix} \dfrac{1}{E_X} & \dfrac{-\nu_{YX}}{E_Y} & 0 \\ \dfrac{-\nu_{XY}}{E_X} & \dfrac{1}{E_Y} & 0 \\ 0 & 0 & \dfrac{1}{G_{XY}} \end{bmatrix}, \tag{12}$$

for which E_X, E_Y are the elastic moduli, G_{XY} is the shear modulus and ν_{XY}, ν_{YX} are the Poisson's ratios with reciprocal relation $\nu_{XY} / E_X = \nu_{YX} / E_Y$. Computed elastic properties for the investigated specimens by means of Eqs. (10)-(12) are listed in Table 1. The present computed values reveal that the investigated specimens have higher stiffness along the *X*-direction compared to the one along the *Y*-direction, i.e. $E_X > E_Y$, which can be explained with the effective deformation mechanisms related to different cell topologies. In other words, over-expanded honeycomb and rectangular cell configurations, which can also be seen in Fig. 12, favor stretch-dominated deformation

along *X*-direction and bending dominated deformation along *Y*-direction, which yields to higher material stiffness along *X*-direction [Deshpande et al., 2001; Alkhader and Vural, 2008].

Furthermore, due to varying number of cells and different topologies for each specimen, there is a large range for the elastic, shear moduli and Poisson's ratios. The variations of these properties are still in good agreement with the computed results by Astley et al. and empirical results by Karakoç et al., Carrington and Cave as tabulated in Table 1 [Astley et al., 1998; Carrington, 1923; Cave, 1969; Karakoç et al., 2013]. Although similar homogenization methods were used for the cell aggregation in both the current and Astley et al. studies, there are slight differences in the results, which is due to the limited number of cells in the investigated specimens where the edge effects are inevitable. In addition, the present model depends upon the assumption of cell wall homogeneity while Astley et al. focused on the use of multi-layer laminates for the cell walls, which is expected to increase the realistic representation for the cell walls.

It is observed from Table 1 that current study overestimates the elastic parameters in comparison with the computed results by Kahle and Woodhouse [Kahle and Woodhouse, 1994]. In this case, different modeling approaches for cellular topologies affect the deformation mechanisms. Kahle and Woodhouse used repetitive irregular hexagonal unit elements in their earlywood investigations, which only focuses on bending deformation and resulting in slightly lower values for elastic properties as seen in Table 1.

Table 1. Near-exact elastic properties for the analyzed Norway spruce earlywood specimens, computed and empirical results obtained from literature, where E_s is the cell wall elastic modulus.

	E_X/E_s	E_Y/E_s	G_{XY}/E_s	ν_{YX}
Present computed results	0.079-0.12	0.029-0.052	0.002-0.006	0.36-0.53
Computed results (repeating irregular hexagons) [Kahle and Woodhouse, 1994]	0.072	0.018	-	0.27
Computed results (skeletised cell geometry) [Astley et al., 1998]	0.067-0.084	0.027-0.043	0.003-0.005	0.40-0.57
Empirical results [Karakoç et al., 2013]	0.106	0.046	0.003	0.27
Empirical results [Carrington, 1923]	0.079	0.048	0.002	0.33
Empirical results [Cave, 1969]	0.071	0.047	0.003	0.29

3.2. Effect of representative volume element size

Wood-like cellular materials have heterogeneous and highly complex structures [Rafsanjani et al., 2012]. For these types of materials, it is well known that influence of chosen RVE size on the effective property is inevitable and RVE size increase is known to result in a converging solution [Nguyen et al., 2012].

In order to understand this phenomenon, effects of cell numbers on the normalized elastic and shear moduli were studied. It can be deduced from Fig. 13 that there is positive linear relation between the cell numbers and elastic moduli for the investigated number of cells. On the other hand, influence of cell numbers seems insignificant in case of shear modulus. However, more investigations on larger number of cell aggregates must be carried out in order to fully support these statements.

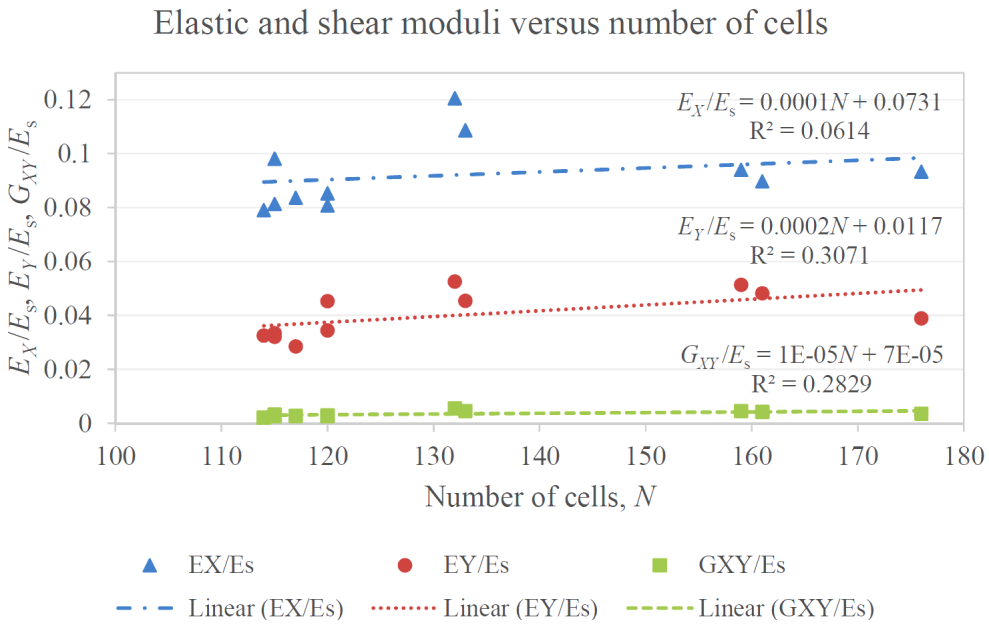

Figure 13: Effect of number of cells on elastic and shear moduli of the analyzed specimens, where E_s is the cell wall elastic modulus.

4. DISCUSSION AND CONCLUSIONS

The present article introduces an algorithm for extracting geometrical data of wood-like

cellular materials in the plane of interest. The output data are expressed in stereolithographic STL format for additive manufacturing and finite element analysis in the homogenization framework.

As explained in the constitutive formulation, three different in-plane loading conditions, tensile load along *X*- and *Y*- directions and *XY*-shear load, were used to compute the transverse elastic properties of Norway spruce earlywood specimens. In total, 11 specimens were investigated to define the elastic property range. It was found out that the tested specimens have higher stiffness along the *X*-direction compared to the one along the *Y*-direction, which is explained with the effective deformation mechanisms related to different cell topologies. The results were then compared with the previous computed and empirical results. The differences between the current and previous studies were presumably due to modelling approaches and specimens with different cell topologies and shapes.

As a result of the introduced algorithm, it is possible to estimate intuitive geometrical and mechanical knowledge for the investigated cellular materials, which increases the efficiency in cellular material research and development. In addition, integration of the algorithm with standard measurement and analysis tools is an advantage in terms of the economic feasibility.

There is also a scope for refinements of the algorithm which currently focuses on material description at cell scale and depends on cell wall homogeneity. For example, it

has a development potential to represent each cell wall as multi-layer laminates, e.g. to mimic softwood cell walls. It is then possible to link and analyze characteristics of cell wall layers and higher material scales, which would result in a more complete solution for multiscale cellular material problems. As elaborated in Table B.1 of Appendix B, mean relative difference for background-to-total pixel area ratios, i.e. cell wall area per total area, between original and reconstructed cellular structures was approximately 13.8% in the current investigations. Therefore, higher order functions with additional intermediate points between consecutive cell vertices are planned to be used in future work to increase the accuracy for cell wall thicknesses. In addition, the algorithm ought to be developed and applied to several cellular material layers along the thickness direction for a complete picture of complex three dimensional materials instead of extruded material profiles (see Fig. 1). Combination of the layer data would enhance the knowledge about the geometries and mechanics of investigated the cellular materials in three dimensional space.

ACKNOWLEDGEMENTS

The authors are thankful for fruitful discussions and supports of Pekka Tukiainen, Prof. Mark Hughes and Prof. Janne Ruokolainen. The authors also gratefully acknowledge the financial support of Multidisciplinary Institute of Digitalisation and Energy (MIDE) through Energy Efficient Wood Processing at Aalto University and Machining Project (E-wood), Puu PostDoc research at Aalto University and the Ministry of Education of Finland through the National Graduate School in Engineering Mechanics. The

computational facilities provided by CSC IT Center for Science, Finland are highly appreciated.

REFERENCES

ABAQUS 2004. Standard User's Manual for Version 6.5.1, Hibbitt, Karlsson and Sorensen Inc.

Alkhader, M., Vural, M., 2008. Mechanical response of cellular solids: Role of cellular topology and microstructural irregularity. International Journal of Engineering Science 46, 1035-1051.

Astley, R.J., Stol, K.A., Harrington, J.J., 1994. Modelling the elastic properties of softwood. Holz als Roh- und Werkstoff 56, 43-50.

Badel, E., Perre, P., 2003. Predicting oak wood properties using X-ray inspection: representation, homogenisation and localisation. Part II: Computation of macroscopic properties and microscopic stress fields. Ann. Forest Sci. 60, 247–257.

Carrington, H., 1923. The elastic properties of spruce. Philosophical Magazine 45, 1055-1057.

Cattaneo, P.M., Dalstra, M., Frich, L.H., 2001. A three- dimensional finite element

model from computed tomography data: a semi-automated method. Proc. Inst. Mech. Eng. 2001, 215, 203-213.

Cave, I., 1969. The longitudinal Young's modulus of Pinus radiate. Wood Sci. Technol. 3, 40-48.

Deshpande, V.S., Ashby, M.F., Fleck, N.A., 2001. Foam topology: bending versus stretching dominated architectures. Acta Materialia 49, 1035-1040.

Farrugia, F., Perre, P., 2000. Microscopic tensile tests in the transverse plane of earlywood and latewood parts of spruce. Wood Sci. Technol. 34, 65-82.

Freund, J., Karakoç, A., Sjölund, J., 2014. Computational homogenization of regular cellular material according to classical elasticity. Mechanics of Materials 78, 56-65.

Gibson, L.J., Ashby, M.F., 1997. Cellular solids: Structure and Properties, second ed. Cambridge University Press.

Iványi, P., 2012. Finite element mesh conversion based on regular expressions. Advances in Engineering Software 51, 20–39.

Kahle, E., Woodhouse, J., 1994. The influence of cell geometry on the elasticity of softwood. J. Mater. Sci. 72, 459-480.

Karakoç, A., Freund, J., 2013. A direct simulation method for the effective in-plane stiffness of cellular materials, International Journal of Applied Mechanics 5 (3), p. 1350034.

Karakoç, A., Tukiainen P., Freund, J., Hughes, M., 2013. Experiments on the effective compliance in the radial-tangential plane of Norway spruce, Composite Structures 102, 287-293.

Kassem, G.A., Weichert D. 2009. Micromechanical material models for polymer composites through advanced numerical simulation techniques. Proc. Appl. Math. Mech. 9, 413-414.

Magne, P., 2007. Efficient 3D finite element analysis of dental restorative procedures using micro-CT data. Dental materials 23, 539-548.

Nguyen, V.D., Bechet, E., Geuzaine, C., Noels, L., 2012. Imposing periodic boundary condition on arbitrary meshes by polynomial interpolation. Computational Materials Science 55, 390-406.

Qing, H., Mishnaevsky, L., 2011. A 3D multilevel model of damage and strength of wood: Analysis of microstructural effects. Mechanics of Materials 43, 487-495.

Rafsanjani, A., Derome, D., Carmeliet, J., 2012. The role of geometrical disorder on swelling anisotropy of cellular solids, Mechanics of Materials 55, 49-59.

Silva, M.J., Gibson, L.J., 1997. The effects of non-periodic microstructure and defects on the compressive strength of two-dimensional cellular solids. Int. J. Mech. Sci. 39, 549-563.

Sjölund, J., Karakoç, A., Freund, J., 2015. Effect of cell geometry and material properties on wood rigidity. International Journal of Solids and Structures 62, 207-216.

Tian, Z., 2013. An algorithm for extracting STL model from axisymmetric ring element mesh. Rapid Prototyping Journal 19, 407-417.

Verdonschot, N., Fennis, W.M., Kuijs, R.H., Stolk, J., Kreulen, C.M., Creugers, N.H., 2001. Generation of 3-D Finite Element Models of Restored Human Teeth Using Micro-CT Techniques. Int J Prosthodont 14, 310-315.

Zdunek, A., Umeda, M., Konstankiewicz, K., 2004. Method of parenchyma cells parameterization using fluorescence images obtained by confocal scanning laser microscope. Electronic Journal of Polish Agricultural Universities 7, #01.

APPENDIX

APPENDIX A. Structure of a Python script for cellular material geometrical modeling in Abaqus/CAE

Here, # stands for numerical value of dimension while (x, y) refers to coordinate data.

```
from abaqus import *
import testUtils
testUtils.setBackwardCompatibility()
from abaqusConstants import *
import sketch
import part

myModel= mdb.Model(name='Model')

mySketch= myModel.ConstrainedSketch(name='Model', sheetSize=#)

xyCoordsOuter =[((x1, y1), ....)]
xyCoordsInner=[((x1, y1), ....)]

for m in range(len(xyCoordsInner)):
for i in range(len(xyCoordsInner[m])-1):
```

```
mySketch.Line(point1=xyCoordsInner[m][i],point2=xyCoordsInner[m][i+1])

for m in range(len(xyCoordsOuter)):
for i in range(len(xyCoordsOuter[m])-1):
mySketch.Line(point1=xyCoordsOuter[m][i],point2=xyCoordsOuter[m][i+1])

(*For the use of two dimensional model*)
myPart=myModel.Part(name='Part',dimensionality=TWO_D_PLANAR,
type=DEFORMABLE_BODY)
myPart.BaseShell(mySketch)

(*For the use of three dimensional model*)
myPart=myModel.Part(name='Part',dimensionality=THREE_D,
type=DEFORMABLE_BODY)
myPart.BaseSolidExtrude(sketch=mySketch, depth=#)

myViewport= session.Viewport(name='Viewport for Model A',
origin=(x, y), width=#, height=#)

myViewport.setValues(displayedObject=myPart)

myViewport.partDisplay.setValues(renderStyle=SHADED)
```

APPENDIX B. Relative difference measure for the background-to-total pixel area ratio between original and reconstructed cellular structures

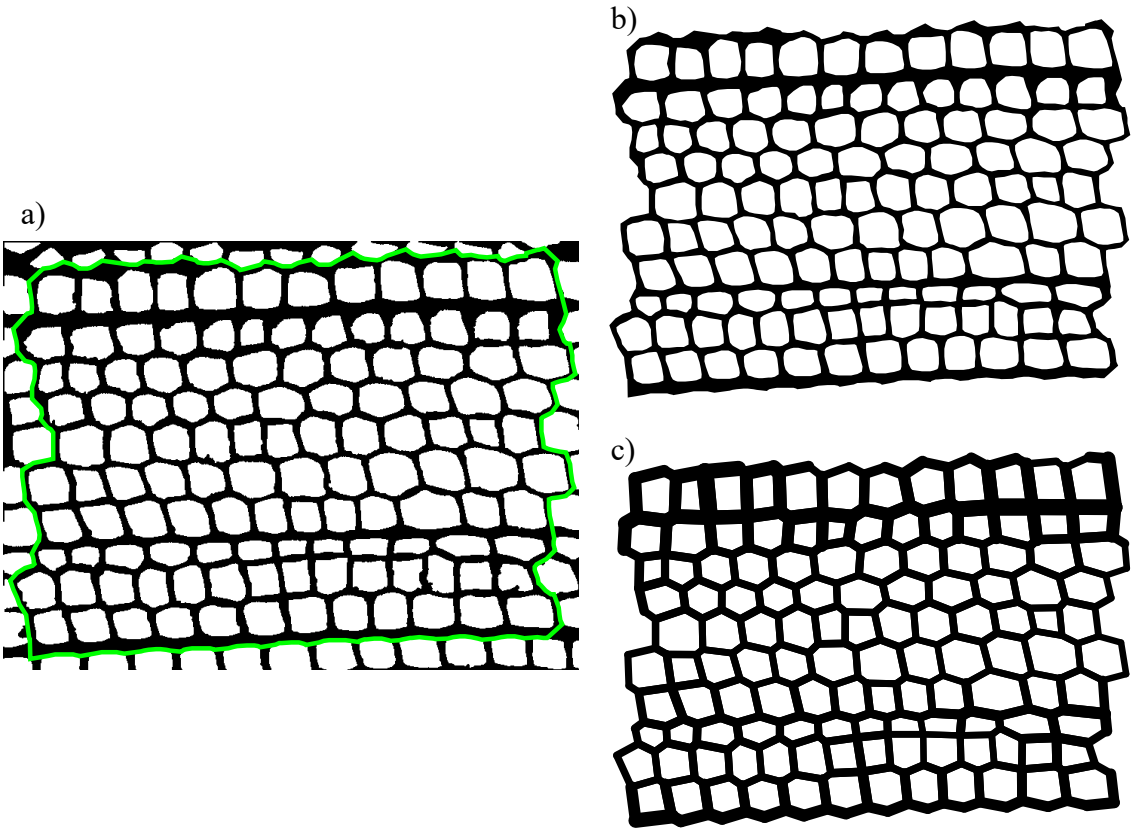

Figure B.1. Original and reconstructed cellular structures: a) original binarized micrograph with the green borderlines showing the region of interest, b) original cropped cellular structure, c) reconstructed cellular structure.

The area ratio for background-to-total pixels for the micrographs can be calculated as

$$AR_{\text{background}} = \frac{A_{\text{background}}}{A_{\text{total}}} \tag{B.1}$$

where relative difference measure follows

$$RD = \frac{\left| AR_{\text{background}}^{\text{reconstructed}} - AR_{\text{background}}^{\text{original}} \right|}{AR_{\text{background}}^{\text{original}}} \tag{B.2}$$

Table B.1: Area ratio $AR_{background}$ and relative difference RD measures for background-to-total pixels for the investigated specimens.

Specimen	$AR_{background}$ for original micrograph	$AR_{background}$ for reconstructed structure	RD
1	0.408	0.468	0.128
2	0.429	0.494	0.132
3	0.419	0.485	0.136
4	0.441	0.510	0.135
5	0.466	0.535	0.129
6	0.359	0.431	0.167
7	0.399	0.465	0.142
8	0.361	0.423	0.147
9	0.360	0.420	0.143
10	0.392	0.445	0.119
11	0.368	0.427	0.138
Min	0.359	0.420	0.119
Max	0.466	0.535	0.167
Mean	0.400	0.464	0.138
Std. Dev.	0.036	0.039	0.012